Nano Research

ISSN 1998-0124 CN 11-5974/O4
https://doi.org/10.26599/NR.2026.94908815

Research Article

Overcoming the thickness scaling limit in hafnium-based ferroelectrics via interfacial strain and conductivity engineering

Bohan Xu[1,2,§](✉), Florian Wunderwald[1,§], Kristina M. Holsgrove[3], Athira Sunil[1], Roberto Guido[1](✉), Julie Laguerre[1], Pramoda Vishnumurthy[1], Xuetao Wang[1], Thomas Mikolajick[1,4], Uwe Schroeder[1](✉)

[1] NaMLab gGmbH, Dresden 01187, Germany

[2] School of Integrated Circuits, Shandong University, Jinan 250100, China

[3] School of Mathematics and Physics, Queen's University Belfast, Belfast BT7 1NN, Northern Ireland, UK

[4] Chair of Nanoelectronics, TU Dresden, Dresden 01187, Germany

[§] Bohan Xu and Florian Wunderwald contributed equally to this work.

Nano Res., **Just Accepted Manuscript** • https://doi.org/10.26599/NR.2026.94908815

https://www.sciopen.com/journal/1998-0124 on May. 6, 2026

© The Authors(s)

Just Accepted

This is a "Just Accepted" manuscript, which has been examined by the peer-review process and has been accepted for publication. A "Just Accepted" manuscript is published online shortly after its acceptance,which is prior to technical editing and formatting and author proofing. Tsinghua University Press (TUP) provides "Just Accepted" as an optional and free service which allows authors to make their results available to the research community as soon as possible after acceptance. After a manuscript has been technically edited and formatted, and the page proofs have been corrected, it will be removed from the "Just Accepted" web site and published officially with volume and article number (e.g., *Nano Research*, **2025**, *18*, 94906990). Please note that technical editing may introduce minor changes to the manuscript text and/or graphics which may affect the content, and all legal disclaimers that apply to the journal pertain. In no event shall TUP be held responsible for errors or consequences arising from the use of any information contained in these "Just Accepted" manuscripts. To cite this anuscript please use its Digital Object Identifier (DOI®),which is identical for all formats of publication.

Just Accepted

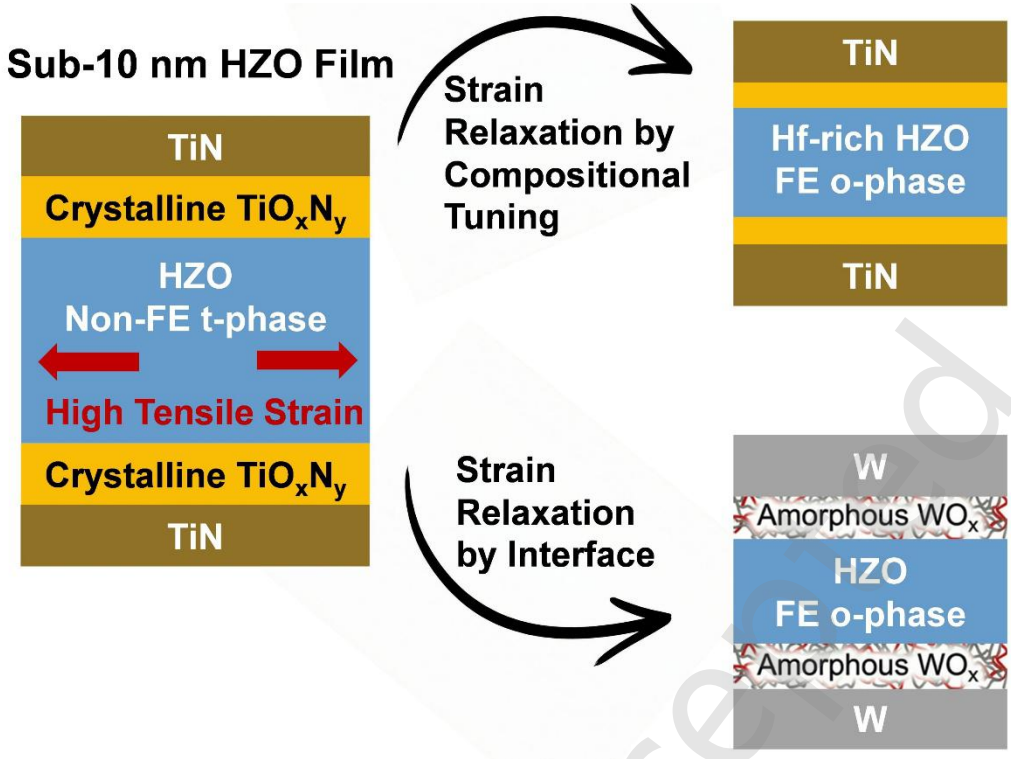

Excessive tensile strain suppresses ferroelectricity in sub-10 nm HZO films with standard TiN electrodes. We demonstrate that the ferroelectric phase can be stabilized through strain relaxation, achieved either by interface engineering using W electrodes or compositional tuning by increasing Hf-content.

Just Accepted

Nano Research

Open Access

Research Article

Overcoming the thickness scaling limit in hafnium-based ferroelectrics via interfacial strain and conductivity engineering

Bohan Xu[1,2,§], Florian Wunderwald[1, §], Kristina M. Holsgrove[3], Athira Sunil[1], Roberto Guido[1], Julie Laguerre[1], Pramoda Vishnumurthy[1], Xuetao Wang[1], Thomas Mikolajick[1,4], and Uwe Schroeder[1]

[1]*NaMLab gGmbH, Dresden 01187, Germany*
[2]*School of Integrated Circuits, Shandong University, Jinan 250100, China*
[3]*School of Mathematics and Physics, Queen's University Belfast, Belfast BT7 1NN, Northern Ireland, UK*
[4]*Chair of Nanoelectronics, TU Dresden, Dresden 01187, Germany*
[§] *Bohan Xu and Florian Wunderwald contributed equally to this work.*

Received: 21 January 2026; **Revised:** 5 May 2026; **Accepted:** 6 May 2026

Address correspondence to Bohan Xu, bohanxu@sdu.edu.cn; Roberto Guido, roberto.guido@namlab.com; Uwe Schroeder, uwe.schroeder@namlab.com

Cite this article: *Nano Research*, 2026, 19, 94908815 https://doi.org/10.26599/NR.2026.94908815

ABSTRACT: Scaling ferroelectric $Hf_{0.5}Zr_{0.5}O_2$ (HZO) films below 10 nm is critical for low-voltage non-volatile memory but remains challenging due to phase instability and interface-related depolarization fields. Here, we demonstrate that the electrode-ferroelectric interface is the key factor for stabilizing the ferroelectric orthorhombic phase in sub-10 nm HZO films. By comparing films down to 5 nm thickness with TiN and W electrodes, we reveal that W electrodes induce significantly lower in-plane tensile strain due to the formation of an amorphous, conductive WO_x interfacial layer. This strain relaxation suppresses the non-polar tetragonal phase favored in ultrathin films, whereas standard TiN electrodes generate high tensile strain that stabilizes the undesirable t-phase. Moreover, the conductive nature of the WO_x layer suppresses the depolarization fields typically caused by dielectric TiO_xN_y interfaces. Consequently, 5 nm HZO films with W electrodes exhibit higher remanent polarization, lower coercive fields, and negligible wake-up effects compared to those with TiN electrodes. Furthermore, we show that the strain-induced performance loss in films with TiN electrodes can be reduced by modifying the Hf:Zr stoichiometry, effectively compensating for the interface strain. These findings establish a critical design rule for interface and strain engineering, providing a pathway to reliable sub-10 nm hafnium-based ferroelectric devices.

KEYWORDS: HZO thin films, ferroelectrics, thickness, electrode, interface, strain

1 Introduction

The scaling of dynamic random-access memory (DRAM) has reached a bottleneck, struggling to meet the demands of modern computing for lower latency and non-volatility [1,2]. This limitation necessitates a transition toward high-density solutions like ferroelectric random-access memory (FeRAM) [3]. The recently discovered fluorite-structured HfO_2-based thin films have emerged as the primary candidate [4,5]. Since fluorite-structured materials like HfO_2 and ZrO_2 are already extensively used in semiconductor manufacturing, HfO_2-based ferroelectrics inherit excellent CMOS compatibility and scalability [2].

However, several problems remain to be addressed before commercial integration. In polycrystalline HfO_2-based thin films, the ferroelectric properties are typically attributed to an orthorhombic phase with a space group of *Pca2₁* (oIII-phase) [6]. Unfortunately, some non-ferroelectric phases, such as the *P2₁/c* monoclinic phase (m-phase), *P4₂/nmc* tetragonal phase (t-phase), and *Pbca* orthorhombic phase (oI-phase), have been commonly reported to be present in the films and have been shown they degrade the ferroelectric properties [7]. Therefore, it is necessary to stabilize the ferroelectric oIII phase throughout the film. In addition to ferroelectric phase stabilization, ferroelectric films should exhibit unlimited electric-field cycling endurance (>10^{15}), a low operating voltage (<1 V), and short latency (<100 ns) to be competitive with current DRAM technology [7,8]. Importantly, reducing the operating voltage below 1 V requires scaling the film thickness, but HfO_2-based films typically lose their ferroelectric properties in this range due to the formation of the non-polar tetragonal phase [9].

Although HfO_2-based thin films have been observed to exhibit their ferroelectric properties even at thicknesses below 10 nm [4], their large coercive field, which is usually more than 1 MV·cm^{-1}, significantly increases the operating voltage when integrated into a 1T-1C FeRAM cell. Since the operating voltage must be at least twice the coercive voltage to induce full polarization reversal [10,11], the film thickness should be scaled down as mentioned above. However, the crystallization temperature typically increases with decreasing film thickness in HfO_2-based films [9]. The

Just Accepted

incorporation of ZrO_2 into HfO_2 has been demonstrated to substantially decrease the crystallization temperature and increase the ferroelectric oIII-phase fraction [12], and the optimal ferroelectric properties are typically exhibited at 50% ZrO_2 content [5].

The electrode material critically influences ferroelectric properties. While different electrodes have been investigated, including TiN, W, Ir, Pt, Ni, Nb, Mo, WO_x, MoO_x, and RuO_x [13–19], TiN and W remain the two most common due to their good thermal stability and CMOS compatibility [3]. However, most investigations of ferroelectric capacitors with TiN or W electrodes have been conducted on films thicker than 10 nm. As the film thickness is reduced, the interfacial layer between the electrode and the ferroelectric film becomes increasingly important.

In this work, we move beyond simple material comparisons to investigate how an interfacial "dead layer" can be transformed into a functional "buffer layer". By comparing films down to 5 nm thickness, we identify a clear difference in performance driven by the mechanical and chemical nature of the electrode interfaces. We demonstrate that the amorphous, conductive WO_x interfacial "buffer layer" formed by W electrodes relieves in-plane tensile strain. This strain relaxation suppresses the non-polar tetragonal phase that typically limits ferroelectric performance. However, to achieve high-performance in ultrathin memory devices, endurance becomes critical. We establish that TiN electrodes, which induce higher strain, can be used effectively at this scale by compensating for the strain through modification of the Hf:Zr stoichiometry. This offers a clear strategy to enable high-performance in ultrathin ferroelectric memory.

2 Experimental

Sample fabrication

On a medium-doped p-type silicon (orientation of (100), resistivity of 1-100 Ω·cm) substrate, either a 10 nm thick titanium nitride (TiN) or tungsten (W) bottom electrode (BE) was deposited at room temperature (RT) via direct current (DC) magnetron sputtering in a BESTEC ultrahigh vacuum chamber. Next, the HZO ferroelectric layer was grown by ALD using an Oxford OpAL system, with C_p-$Zr[N(CH_3)_2]_3$ (ZyALD) and C_p-$Hf[N(CH_3)_2]_3$ (HyALD) as metal-organic precursors, and ozone as the oxidant. The different thicknesses of the HZO films (from 5 to 15 nm) were achieved by varying the number of ALD cycles. Then, either a 10 nm thick TiN or W top electrode (TE) was deposited in the same BESTEC chamber. Subsequently, rapid thermal annealing (RTA) was performed at a temperature of 450°C for 20 seconds, with a heating rate of 25 K/s. This process was conducted using an Annealsys AS Master 2000 furnace. The process temperatures were maintained below 450°C for all the capacitor stacks to ensure the compatibility with BEOL processing. The capacitor structure was patterned through sequential lithographic and etching processes. First, laser lithography was performed using a Heidelberg Instruments μPG 101 system. A bilayer stack of titanium (10 nm) and platinum (25 nm) was then deposited in a BESTEC electron-beam evaporation tool, followed by lift-off in acetone under an ultrasonic bath. Finally, inductively coupled plasma (ICP) reactive ion etching (Oxford Instruments Plasmalab System133) was used to structure the top electrode. The capacitor stacks utilized in this study are illustrated in the Electronic Supplementary Material (**Figure S1**).

Characterization

The electrical measurements were performed using a Cascade Microtech Summit 12000 probe station and Keithley 4200SCS analyzer. Moreover, an aixACCT TF 3000 ferroelectric analyzer was used to apply square electrical pulses to cycle the capacitors. The capacitor area was approximately 1960 μm^2.

Impedance spectroscopy was performed using a 100 mV AC signal with zero DC bias, ranging from 1 Hz to 5 MHz, with a Load-Load-Load compensation sequence in an MFIA impedance analyzer by Zurich Instruments. Electrical equivalent circuit modelling of measured HZO capacitors and fitting was performed using ZView software by Scribner.

GIXRD and BBXRD were performed using a Bruker D8 Discover instrument with Cu-Kα radiation (wavelength 0.154 nm).

A Tescan focused ion beam (FIB)-secondary electron microscope (SEM) Lyra 3 was used to prepare cross-sectional lamellae for transmission electron microscopy. FIB milling was performed with gallium ions at accelerating voltages of 30 kV (rough milling) and 5, 2, and 1 kV (fine polishing). Scanning Transmission Electron Microscopy was performed on a ThermoFisher Scientific Talos F200X instrument fitted with a Super-X energy-dispersive X-ray spectrometer (EDX) operated at a 200 kV accelerating voltage. For differential phase contrast (DPC) – STEM imaging, a segmented detector (ThermoFisher) was used, a beam convergence angle of 7.5 mrad, and a camera length of 260mm was applied. These conditions provided DPC-STEM images dominated by diffraction contrast, aiding the identification of interfacial layers.

3 Results and discussion

As demonstrated in **Figures 1(a)** and **1(b)**, grazing incidence X-ray diffraction (GIXRD) measurements reveal the coexistence of the non-polar m-phase with the oIII-/t-phases for films thicker than 10 nm, regardless of the electrode material. The m-phase is suppressed by decreasing the film thickness, and it disappears in films thinner than 10 nm. Distinguishing the fraction of the ferroelectric oIII-phase from the non-polar t- phase by GIXRD is usually difficult due to the similarity of the lattice constant between these two phases [20]. It has been recently reported that the largest oIII-phase fraction in HZO films can be achieved for about 0.4-0.5% in-plane tensile strain, and that exceeding this in-plane tensile strain threshold is often indicative of a large amount of the non-polar t-phase [21,22]. Therefore, the in-plane tensile strain in the HfO_2-based thin films can help determine the fraction of the ferroelectric oIII-phase. The in-plane tensile strains were determined through Bragg-Brentano X-ray diffraction (BBXRD) and the $\sin^2\Psi$ method. More details about these measurements are discussed in the Electronic Supplementary Material (**Section S2**). The in-plane tensile strain for the HZO films with different thicknesses and electrodes is shown in **Figure 1(c)**. For HZO films with TiN electrodes, the in-plane tensile strain reaches

Just Accepted

a maximum at 5 nm HZO, then decreases from 0.73% to 0.5-0.45% as the film thickness increases to 15 nm. This outcome suggests that t-phase stabilization is enhanced in ultrathin films. This experimental result was confirmed by DFT simulation results, indicating that for HZO films with a thickness above 10 nm the o-phase has the lowest free energy, and the t-phase is preferred from an energetic point of view in films thinner than 10 nm [6]. For HZO films with W electrodes exhibit a smaller in-plane tensile strain compared to that obtained when using TiN electrodes with an almost constant strain value of 0.36% to 0.39% for the complete film thickness range from 5 to 15 nm. This result indicates that a lower non-polar t- and higher ferroelectric oIII-phases are expected in 5 nm thick HZO films with W electrodes compared to the TiN electrode case. Similar trends are observed using cross-sectional high-resolution transmission electron microscopy. For the TiN/HZO capacitors, the (002) lattice spacing of the oIII-phase is measured as 2.54 Å, and corresponds to a 0.71% tensile strain (**Figure 1(d)**). **Figure 1(d)** shows that oxidation of TiN at the interface to HZO does not drastically impact the crystalline structure of the interface layer at the bottom electrode. Indeed, a clear orientational alignment between the atomic planes within the grains of the TiN interface and HZO is visible. Such a clamping imposed by the TiN electrodes on the HZO can explain the strain increase in the ferroelectric film. For the HZO capacitors with W electrodes, the (111) lattice spacing of the oIII-phase is 2.95 Å, which translates into a tensile strain of 0.50% (**Figure 1(e)**).

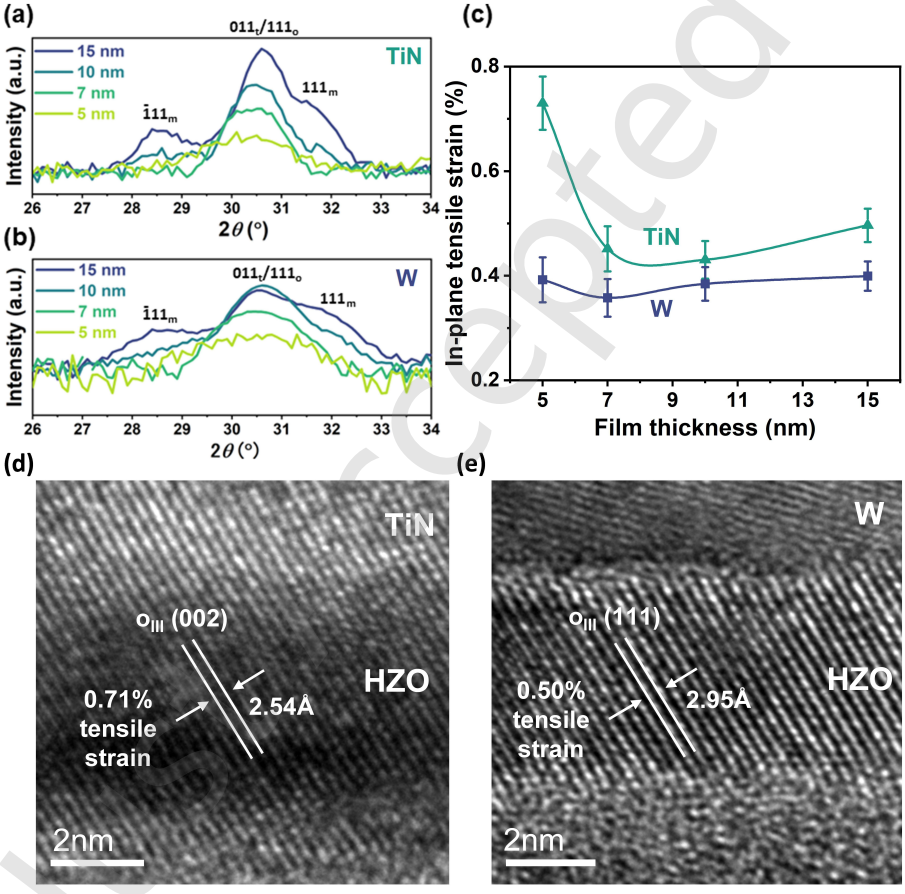

Figure 1 Grazing incidence X-ray diffraction (GIXRD) measurements (in log scale) on HZO films with thicknesses from 5 nm to 15 nm for HZO films with (a) TiN and (b) W electrodes. (c) In-plane tensile strain versus film thickness for HZO films with TiN and W electrodes. Cross-sectional high-resolution transmission electron microscopy images of 5 nm thick HZO film with (d) TiN electrodes and (e) W electrodes. For both electrodes, the tensile strain is determined by comparing the HZO lattice spacings to bulk reference values.

The different strains can result from several parameters during processing, such as lattice mismatch of HZO with the electrodes [23], coefficient of thermal expansion (CTE) difference between HZO and electrode [24], capping effect from the top electrode [25], and film densification and crystallization from the amorphous phase during annealing [26]. It is critical to distinguish the magnitude and contribution of two strain sources in HZO films: the densification strain generated during crystalline phase formation, and the thermal stress induced by CTE mismatch during post-annealing cooling. The densification upon t-phase crystallization introduces a large in-plane tensile strain exceeding 0.4% (~1 GPa stress), which dominates the strain state of the HZO film. This value can be reduced if t-phase further transitions to the o-phase or m-phase, due to their larger unit cell volumes compared to the t-phase. In contrast, the thermal strain from CTE mismatch only contributes a stress on the MPa scale, which is negligible compared to the densification-induced strain.

Based solely on CTE values, the W electrode exhibits a larger CTE than the TiN electrode, which should theoretically induce a larger in-plane tensile strain in the HZO film. However, this theoretical expectation contradicts our experimental observation in this work. This discrepancy is

attributed to two key factors. Firstly, the dominant densification strain overwhelms the minor thermal stress difference between W and TiN electrodes. Secondly, the strain relaxation likely arises from the amorphous WO_x interfacial layer. During high-temperature annealing, W electrodes form an amorphous WO_x layer at the interface with HZO, which acts as a buffer layer to release the interfacial strain between W and HZO.

In addition to phase stabilization influenced by in-plane tensile strain, the interfacial layer is another critical factor that affects the electrical behavior of ferroelectric HfO_2-based thin films. Due to incomplete charge screening, the dielectric interfacial layer can generate a depolarization field, weakening the ferroelectric properties of the films and introducing a pinched hysteresis loop [27,28]. An interfacial layer is clearly observed in the cross-sectional differential phase contrast scanning transmission electron microscopy (DPC-STEM) image of the 5 nm thick HZO film with TiN electrodes (**Figure 2(a)**). The composition of this interfacial layer is usually TiO_xN_y [29], which can be either conductive or dielectric. Impedance spectroscopy reveals the dielectric nature of the TiO_xN_y interface layer, as shown in **Figure 2(c)**. Assuming a dielectric constant of 10 for the interfacial layer, the effective thickness of this interfacial layer is determined to be 2.2 ± 0.1 nm. More details on determining the interfacial layer thickness are shown in the Electronic Supplementary Material (**Section S3**). This interface layer thickness value aligns well with the 2 nm value extracted from the DPC-STEM image in **Figure 2(a)**. The formation of the interfacial layer is primarily attributed to the oxidation of the TiN bottom electrode during atomic layer deposition (ALD) of the HZO layer and the subsequent annealing process. In general, higher processing temperatures result in a thicker interfacial layer [28]. Consequently, preventing the formation of this interfacial layer while providing sufficient thermal budget to stabilize the oIII-phase in such thin films is challenging.

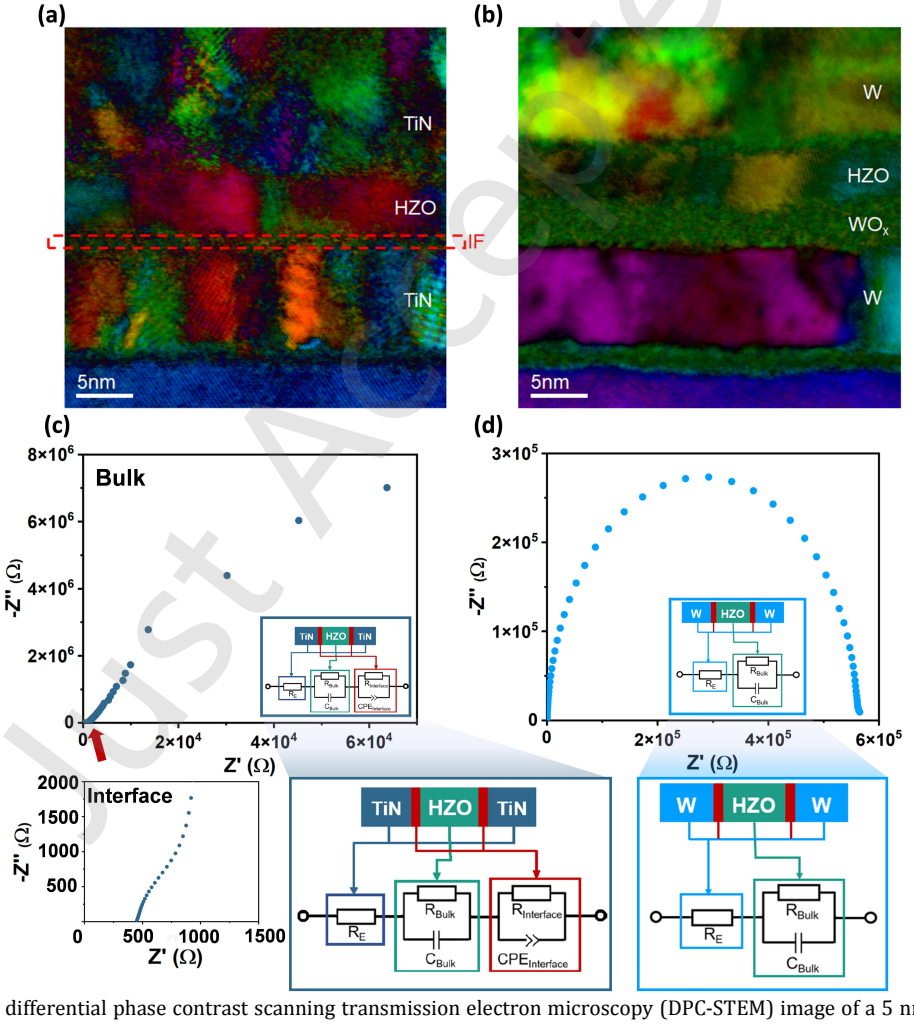

Figure 2 Cross-sectional differential phase contrast scanning transmission electron microscopy (DPC-STEM) image of a 5 nm thick HZO film with (a) TiN electrodes and (b) W electrodes. (c) Imaginary part versus real part of the impedance (Nyquist plot) of a 5 nm thick HZO film with TiN electrodes. A zoom into the low impedance area is shown below the graph. (d) Nyquist plot of a 5 nm thick HZO film with W electrodes. A sketch of the equivalent circuit for modeling the capacitor stack is reported in the insets of (c) and (d).

As demonstrated by DPC-STEM measurements in **Figure 2(b)**, an approximately 3.5 nm thick WO_x interfacial layer is formed between the 5 nm thick HZO film and the bottom W electrodes, mainly during HZO deposition. The interface layer formed during crystallization anneal is thinner at the W top electrode, for instance, in **Figure 2(b)**, only about 1 nm WO_x is observed at the top interface. However, in contrast to the TiO_xN_y layer, the impedance spectroscopy analysis shown in **Figure 2(d)** points out that the WO_x layer remains conductive. The conductivity of the WO_x layer can

Just Accepted

be attributed to oxygen deficiency [14]. More detailed characterization of the interfacial layer compositions is reported in the Electronic Supplementary Material (**Figure S2**).

In summary, the use of either TiN or W electrodes eliminates the presence of the non-polar m-phase in HZO films thinner than 10 nm. The lower in-plane tensile strain for HZO films with W electrodes suggests a reduced non-polar t-phase fraction. Furthermore, the interfacial layers formed are different when using TiN and W electrodes. The TiO_xN_y interfacial layer detected between HZO and TiN is crystalline and shows a dielectric nature, whereas the amorphous WO_x interfacial layer formed between HZO and W is conductive.

As shown in **Figure 3(a)**, the switching current peak in the pristine state of HZO films with TiN electrode starts to split into two peaks when reducing the film thickness from 15 to 5 nm, and a larger applied electric field magnitude is required to reverse the polarization or induce a field-induced phase change. The peak splitting is likely due to the higher t-phase content in thinner films, since DFT simulations predicted the t-phase as the most stable phase for films below 10 nm [6,13]. The non-polar t-phase can transition to the ferroelectric oIII-phase by applying a sufficiently large electric field, but a back transition to the t-phase is induced upon the removal of the electric field [30–32]. These two phase transitions give rise to two current peaks, and consequently, a pinched polarization hysteresis loop. Additionally, the dielectric TiO_xN_y interfacial layer generates a depolarization field that can further contribute to peak splitting and pinched hysteresis loops [27,28]. Field cycling can induce wake-up effects. Several factors contribute to this wake-up effect, including field-induced irreversible t- to oIII-phase transition, strain relaxation, ferroelastic domain switching, and defect redistribution [26,33–38]. However, such wake-up effects are undesirable for ferroelectric memory devices since they require pre-cycling each device before its actual use [39]. As illustrated in **Figure 3(c)**, the switching field starts to merge and shift to a lower field after 10^5 cycles in 5 nm HZO films, and a strong wake-up behavior is observable in **Figure 3(e)**.

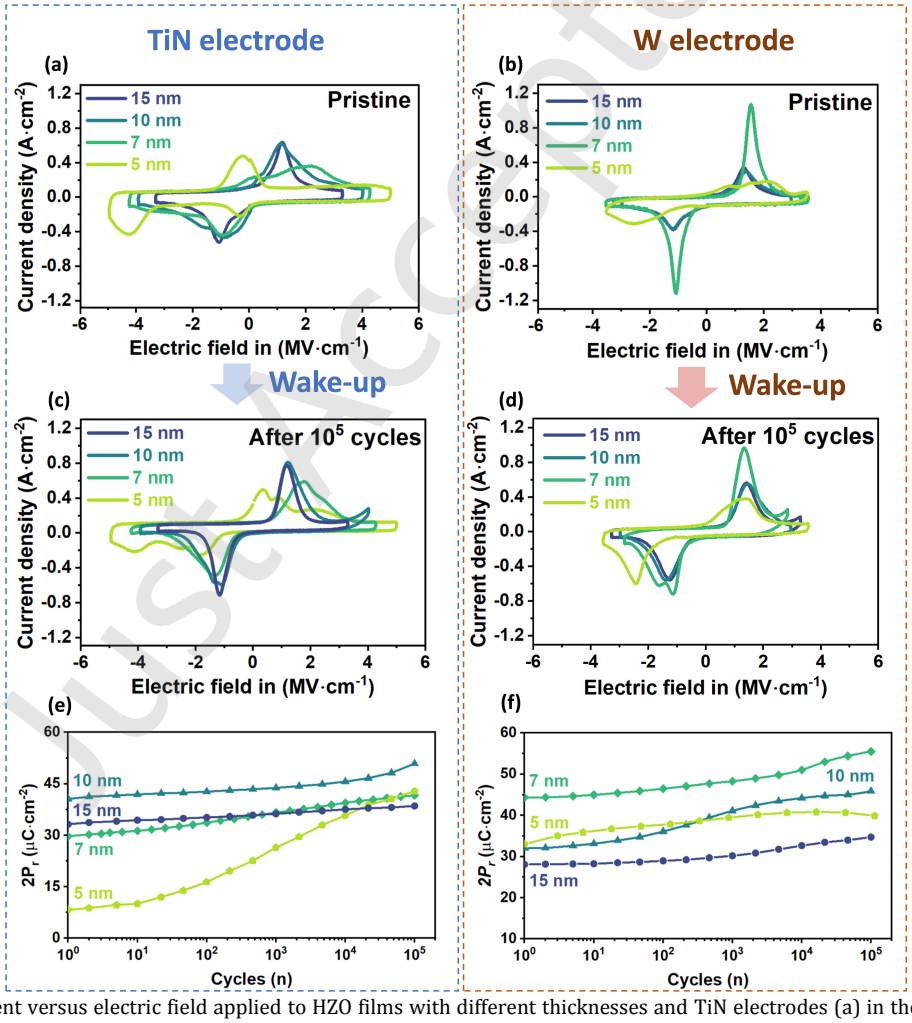

Figure 3 Transient current versus electric field applied to HZO films with different thicknesses and TiN electrodes (a) in the pristine state of the film and (c) after 10^5 electric field cycling. Transient current versus electric field applied to HZO films W electrodes (b) in the pristine state of the film and (d) after 10^5 electric field cycling. Two times remanent polarization ($2P_r$) versus number of electrical cycles for HZO films with different film thicknesses and (e) TiN or (f) W electrodes. Measurements were performed at a frequency of 1 kHz on capacitors with an area of 9500 μm^2.

Figure 3(b) shows that the coercive fields shift to higher values when the film thickness is less than 7 nm, and a peak splitting appears in 5 nm HZO films with W electrodes. However, in contrast to films with TiN electrodes, the switching current peaks merge after electric field cycling for the 5 nm HZO film with W electrodes, as shown in **Figure 3(d)**. Moreover, the 5 nm HZO film with W electrodes exhibits strong ferroelectric behavior without the

Just Accepted

requirement for additional wake-up procedures, as illustrated in **Figure 3(f)**. As indicated by the structural characterization, stabilizing the t-phase in the 5 nm thick HZO film with W electrodes reduces the $2P_r$. These results are consistent with the outcomes of the previous investigation, which found that coercive fields increase with larger in-plane tensile strain, or that the electric field at which a field-induced phase transition occurs increases [28]. Although the ferroelectric properties of HZO films with the W electrodes begin to degrade at 5 nm, they still exhibit significantly better performances than those of the same thickness and TiN electrodes. Moreover, HZO films with W electrodes require a lower electric field to initiate domain switching. However, they exhibit worse endurance than those with TiN electrodes. More details are discussed in the Electronic Supplementary Material (**Section S4**). Furthermore, in contrast to the HZO films with the TiN electrodes, which achieve the largest P_r values at 10 nm, as reported in other publications [9,40], the HZO films with the W electrodes demonstrate the largest P_r values for the thickness of 7 nm. In addition to the transient currents, more details of the polarization hysteresis loops are illustrated in **Figure S7**.

In general, the lower in-plane tensile strain and the conductive WO_x interfacial layer imply better ferroelectric properties in the HZO ultrathin films with W electrodes than films with TiN electrodes, including almost absent wake-up behavior.

A similar behavior is present when comparing the $2P_r$ for both electrodes while correlating it with the in-plane tensile strain (**Figure 4a**). Best $2P_r$ values of 35-45 μC·cm^{-2} are obtained in the strain range between 0.35-0.45% with a clear drop in polarization for higher strain values. Here, a higher t-phase content is expected, which is supported by electric field measurements (**Figure 4b**). The E_c is approximately 1.1 MV·cm^{-1} over the strain range of 0.35–0.45%. A further increase in strain to 0.73% leads to peak splitting and a field-induced transition from the t- to oIII-phase with enhanced transition fields of 4 MV·cm^{-1}. Therefore, the term switching field is used instead of coercive field, because the electric-field-induced phase transition also occurs in some films, in addition to domain switching.The linear correlation between the switching field and strain is discussed in more detail in our previous investigations [22]. Overall, as illustrated in **Figures 3(c)** and **3(d)**, the E_c range (ΔE_c, as the full width half maximum of the ferroelectric switching peak) for switching is narrower for W electrodes with ΔE_c values of about 0.6 MV·cm^{-1}, slightly increasing to 1 MV·cm^{-1} for the 5 nm HZO case. For TiN electrodes, the ΔE_c values increase above 1 MV·cm^{-1} for HZO thickness values below 10 nm. Higher t-phase portions cause peak splitting, which is often indicated by peak broadening. Additionally, the formation of the t-phase and the particular interfacial layer nature cause a significant drop of $2P_r$ in 5 nm films with TiN electrodes.

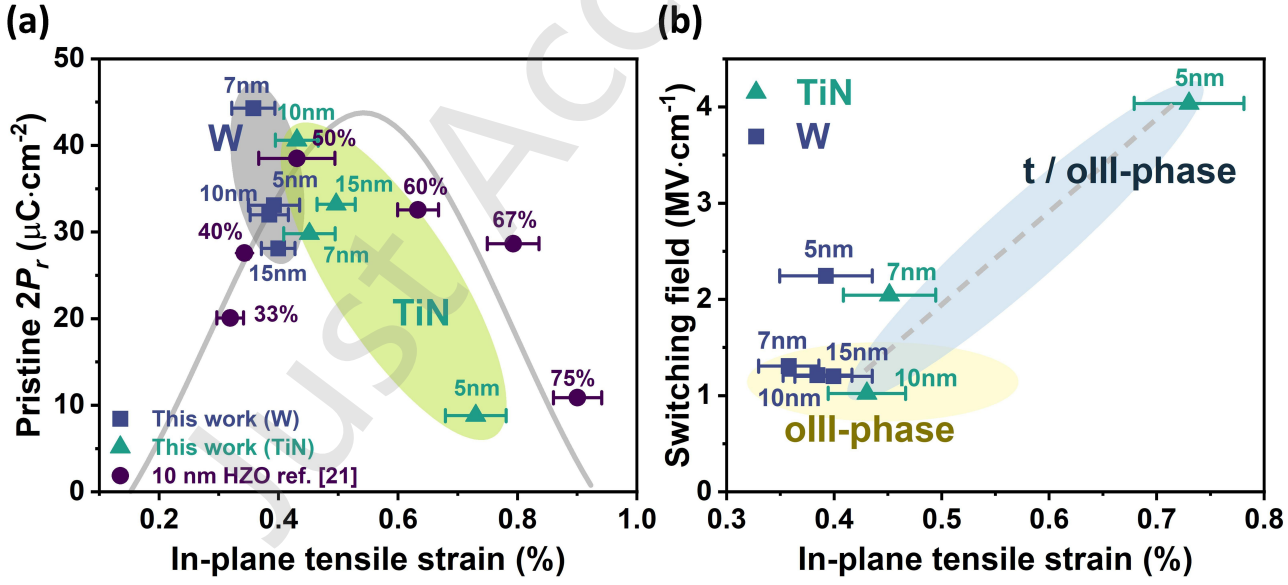

Figure 4. (a) Pristine $2P_r$ and (b) coercive field E_c or t- to oIII-switching field as a function of in-plane tensile strain for both electrodes.

These results clearly indicate that a strain reduction is necessary to improve $2P_r$ when using TiN electrodes. As shown by the filled circles data points in **Figure 4(a)**, Wunderwald et al. reported that strain can be effectively reduced by enhancing the Hf-content in 10 nm HZO layers [21]. As illustrated in **Figure 5(a)**, increasing Hf-content from 50% to 56% can improve the $2P_r$ from 9 to 17 μC·cm^{-2} in the pristine state of the 5 nm HZO film with the TiN electrodes [41], and a stable $2P_r$ of 50 μC·cm^{-2} after 10^5 cycles is achievable. As illustrated in **Figure 5(b)**, this enhancement in polarization correlates with the strain reduction from 0.73 to 0.69% resulting from the increased Hf-content. Moreover, based on our previous study, increasing the Hf-content also reduces the thickness of the interfacial layer in ultrathin HZO films [42].

For W electrodes, the pristine $2P_r$ values for 5 nm HZO decrease from 33 to 19 μC·cm^{-2} by increasing the Hf-content of the same amount. Such $2P_r$ reduction is due to the further reduction of in-plane tensile strain from 0.39% to 0.23%, which is too low to have a high oIII-phase content in the 5 nm HZO films. Therefore, such a strain decrease shifts the properties away from the optimal range of strain values

Just Accepted

required for achieving the largest $2P_r$.

Overall, the ferroelectric properties of ultrathin HZO films with W electrodes in the pristine state are a direct consequence of the relatively low in-plane tensile strain, which is correlated with the amorphous and conductive nature of the WO_x interfacial layer. When using TiN electrodes, similar performance can be achieved by increasing the Hf-content in the HZO film, thereby reducing in-plane tensile strain. For both electrodes, the change in $2P_r$ with strain follows the trend previously determined for 10 nm HZO films on TiN electrodes, as illustrated in **Figure 5(b)** [21].

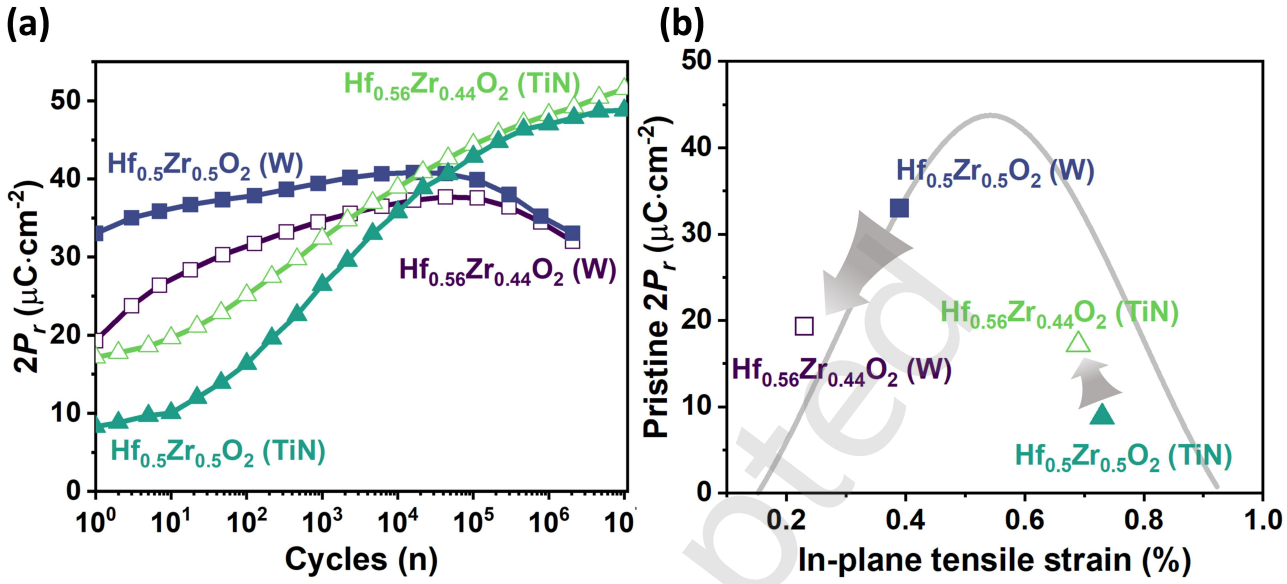

Figure 5. (a) $2P_r$ versus number of electrical cycles for 5 nm thick HZO films with different Hf-content and TiN and W electrodes [41]. (b) Pristine $2P_r$ for 50% and 56% HfO_2 content in HZO a function of in-plane tensile strain for both electrodes.

In summary, the better ferroelectric performance of ultrathin HZO films with W electrodes is a direct result of reduced in-plane tensile strain, enabled by the amorphous, conductive WO_x interface. For TiN electrodes, which typically induce higher, undesirable strain levels, it is shown that comparable performance can be achieved by increasing the Hf-content to mechanically relax the strain. Remarkably, regardless of the approach, the relationship between $2P_r$ and strain follows the same universal trend, as illustrated in **Figure 5(b)**. This confirms that in-plane strain is the fundamental factor governing phase stability in the sub-10 nm range, and that maintaining it within the optimal window (0.3%–0.5%) is essential for high-performance sub-10 nm devices.

4 Conclusions

This study establishes that the electrode interface is not merely an electrical contact but a mechanical template that determines phase stability in the sub-10 nm range. We have shown that the failure of standard TiN electrodes in sub-10 nm HZO arises from excessive in-plane tensile strain, which energetically favors the non-polar tetragonal phase, combined with a dielectric TiO_xN_y "dead layer". In contrast, W electrodes enable robust ferroelectricity at 5 nm by forming a conductive, amorphous WO_x "buffer layer" that relaxes strain and screens depolarization fields.

These findings provide a clear design strategy for future FeRAM technology where scaling below 10 nm requires either using electrodes that permit strain relaxation or compensating for electrode-induced strain via compositional tuning. This strain-interface coupling mechanism resolves the trade-off between scaling and ferroelectric performance, enabling the integration of high-density, low-voltage ferroelectric memories into advanced CMOS nodes. Since the W electrode exhibits earlier breakdown during field cycling, this paper discusses strain-improvement paths for TiN electrodes to achieve stable polarization and enhanced field cycling endurance in improved film stacks.

Electronic Supplementary Material: Supplementary material (Section S1: Sketch of the capacitor structures; Section S2: Bragg-Brentano Strain Measurements; Section S3: Interfacial Layer Determination; Section S4: Field Cycling Endurance) is available in the online version of this article at https://doi.org/10.26599/NR.2026.94908815.

Data availability

All data needed to support the conclusions in the paper are presented in the manuscript and/or the Electronic Supplementary Material. Additional data related to this paper may be requested from the corresponding author upon request.

Acknowledgements

B.X., R.G., and F.W. were financially supported by the Deutsche Forschungsgemeinschaft (DFG) within the following projects (D3PO (505873959), WUMM (458372836), and Zeppelin (433647091)). K.M.H. was financially supported by the Department of Education and Learning NI through grant USI-205. J.L. received funding from the Sächsische Aufbaubank (SAB project 'Leistungsschalter'). P.V. was financially supported by Samsung Electronics Co., Ltd. X.W., T.M., and U.S. were financially supported out of the Saxonian State budget approved by the delegates of the Saxon State Parliament. B.X.'s work was partially financially supported by the European Union's Horizon 2020 research and innovation program under grant agreement No 101016776 (FVLLMONTI) and Young Scientist Supporting Project

Just Accepted

(11500061330000).

Declaration of competing interest

All the contributing author(s) report(s) no conflict of interests in this work.

Author contribution statement

B.X.: Conceptualization, formal analysis, investigation, methodology, supervision, writing manuscript. F.W.: Formal analysis, investigation, validation, writing – review & editing. K.M.H.: Formal analysis, investigation, writing manuscript. A.S.: Formal analysis, investigation. R.G.: Conceptualization, methodology, writing – review & editing. J.L.: Formal analysis, investigation. P.V.: Formal analysis, investigation, writing – review & editing. X.W.: Methodology. T.M.: Funding acquisition, project administration, resources, supervision, writing – review & editing. U.S.: Conceptualization, funding acquisition, project administration, resources, supervision, writing – review & editing. All the authors have approved the final manuscript.

Use of AI statement

None.

References

[1] Mikolajick, T.; Park, M. H.; Begon-Lours, L.; Slesazeck, S. From Ferroelectric Material Optimization to Neuromorphic Devices. *Advanced Materials* **2023**, *35*, 2206042.

[2] Schenk, T.; Pešić, M.; Slesazeck, S.; Schroeder, U.; Mikolajick, T. Memory technology—a primer for material scientists. *Reports on Progress in Physics* **2020**, *83*, 086501.

[3] Silva, J. P. B.; Alcala, R.; Avci, U. E.; Barrett, N.; Bégon-Lours, L.; Borg, M.; Byun, S.; Chang, S.-C.; Cheong, S.-W.; Choe, D.-H.; et al. Roadmap on ferroelectric hafnia- and zirconia-based materials and devices. *APL Materials* **2023**, *11*, 089201.

[4] Böscke, T. S.; Müller, J.; Bräuhaus, D.; Schröder, U.; Böttger, U. Ferroelectricity in hafnium oxide thin films. *Appl. Phys. Lett.* **2011**, *99*, 102903.

[5] Müller, J.; Böscke, T. S.; Schröder, U.; Mueller, S.; Bräuhaus, D.; Böttger, U.; Frey, L.; Mikolajick, T. Ferroelectricity in Simple Binary ZrO_2 and HfO_2. *Nano Lett.* **2012**, *12*, 4318–4323.

[6] Materlik, R.; Künneth, C.; Kersch, A. The origin of ferroelectricity in $Hf_{1-x}Zr_xO_2$: A computational investigation and a surface energy model. *Journal of Applied Physics* **2015**, *117*, 134109.

[7] Schroeder, U.; Park, M. H.; Mikolajick, T.; Hwang, C. S. The fundamentals and applications of ferroelectric HfO_2. *Nature Reviews Materials* **2022**, *7*, 653–669.

[8] Mikolajick, T.; Slesazeck, S.; Mulaosmanovic, H.; Park, M. H.; Fichtner, S.; Lomenzo, P. D.; Hoffmann, M.; Schroeder, U. Next generation ferroelectric materials for semiconductor process integration and their applications. *Journal of Applied Physics* **2021**, *129*, 100901.

[9] Park, M. H.; Lee, Y. H.; Kim, H. J.; Schenk, T.; Lee, W.; Kim, K. D.; Fengler, F. P. G.; Mikolajick, T.; Schroeder, U.; Hwang, C. S. Surface and grain boundary energy as the key enabler of ferroelectricity in nanoscale hafnia-zirconia: a comparison of model and experiment. *Nanoscale* **2017**, *9*, 9973–9986.

[10] Fu Z.; Yang M.; Wang K.; Huang Q.; Huang R. New Understanding of Memory Window Reduction Induced by Ferroelectric Dynamics for HfO_2-based 1T1C FeRAM. *2023 Silicon Nanoelectronics Workshop (SNW)* **2023**, , 55–56.

[11] Chang K. -C.; Chen P. -H.; Chang T. -C.; Tan Y. -F.; Chen W. -C.; Yeh C. -H.; Ciou F. -M.; Tai M. -C.; Tsai T. -M.; Sze S. A Method to Measure Polarization Signal of Nanoscale One-Transistor-One-Capacitor Ferroelectric Memory. *IEEE Electron Device Letters* **2022**, *43*, 862–865.

[12] Hsain, H. A.; Lee, Y.; Parsons, G.; Jones, J. L. Compositional dependence of crystallization temperatures and phase evolution in hafnia-zirconia (Hf_xZr_{1-x})O_2 thin films. *Applied Physics Letters* **2020**, *116*, 192901.

[13] Alcala, R.; Materano, M.; Lomenzo, P. D.; Vishnumurthy, P.; Hamouda, W.; Dubourdieu, C.; Kersch, A.; Barrett, N.; Mikolajick, T.; Schroeder, U. The Electrode-Ferroelectric Interface as the Primary Constraint on Endurance and Retention in HZO-Based Ferroelectric Capacitors. *Advanced Functional Materials* **2023**, *33*, 2303261.

[14] Wang, X.; Slesazeck, S.; Mikolajick, T.; Grube, M. Modulation of Oxygen Content and Ferroelectricity in Sputtered Hafnia-Zirconia by Engineering of Tungsten Oxide Bottom Electrodes. *Advanced Electronic Materials* **2024**, *10*, 2300798.

[15] Kashir, A.; Kim, H.; Oh, S.; Hwang, H. Large Remnant Polarization in a Wake-Up Free $Hf_{0.5}Zr_{0.5}O_2$ Ferroelectric Film through Bulk and Interface Engineering. *ACS Appl. Electron. Mater.* **2021**, *3*, 629–638.

[16] Fields, S. S.; Smith, S. W.; Jaszewski, S. T.; Mimura, T.; Dickie, D. A.; Esteves, G.; David Henry, M.; Wolfley, S. L.; Davids, P. S.; Ihlefeld, J. F. Wake-up and fatigue mechanisms in ferroelectric $Hf_{0.5}Zr_{0.5}O_2$ films with symmetric RuO_2 electrodes. *Journal of Applied Physics* **2021**, *130*, 134101.

[17] Park, M. H.; Kim, H. J.; Kim, Y. J.; Lee, W.; Moon, T.; Kim, K. D.; Hwang, C. S. Study on the degradation mechanism of the ferroelectric properties of thin $Hf_{0.5}Zr_{0.5}O_2$ films on TiN and Ir electrodes. *Applied Physics Letters* **2014**, *105*, 072902.

[18] Park, J. Y.; Choi, H.; Lee, J.; Yang, K.; Lee, S. Y.; Han, D. I.; Jeon, I.; Jung, C. H.; Lim, H.; Lee, W.; et al. Enhancement of electrical properties of morphotropic phase boundary in $Hf_{1-x}Zr_xO_2$ films by integrating Mo electrode and TiN interlayer for DRAM capacitors. *Applied Surface Science Advances* **2025**, *27*, 100733.

[19] Zhao R.; Liu T.; Zhao X.; Liu H.; Shao M.; Feng Q.; Sun X.; Wu X.; Yang Y.; Ren T. -L. Impact of Molybdenum Oxide Electrode on the Ferroelectricity of Doped-Hafnia Oxide Capacitors. *IEEE Transactions on Electron Devices* **2022**, *69*, 1492–1496.

[20] Schroeder, U.; Sachdeva, R.; Lomenzo, P. D.; Xu, B.; Materano, M.; Mikolajick, T.; Kersch, A. Using Raman spectroscopy and x-ray diffraction for phase determination in ferroelectric mixed $Hf_{1-x}Zr_xO_2$-based layers. *Journal of Applied Physics* **2022**, *132*, 214104.

[21] Wunderwald, F.; Xu, B.; Kersch, A.; Holsgrove, K. M.; Kao, Y.-C.; Richter, C.; Enghardt, S.; Mikolajick, T.; Schroeder, U. Interaction Between Strain and Phase Formation in $Hf_xZr_{1-x}O_2$ Thin Films. *Small* **2025**, *21*, 2408133.

[22] Xu, B.; Lomenzo, P. D.; Kersch, A.; Schenk, T.; Richter, C.; Fancher, C. M.; Starschich, S.; Berg, F.; Reinig, P.; Holsgrove, K. M.; et al. Strain as a Global Factor in Stabilizing the Ferroelectric Properties of ZrO_2. *Advanced Functional Materials* **2024**, *34*, 2311825.

[23] Song, T.; Lenzi, V.; Silva, J. P. B.; Marques, L.; Fina, I.; Sánchez, F. Disentangling stress and strain effects in ferroelectric HfO_2. *Applied Physics Reviews* **2023**, *10*, 041415.

[24] Goh, Y.; Hwang, J.; Lee, Y.; Kim, M.; Jeon, S. Ultra-thin $Hf_{0.5}Zr_{0.5}O_2$ thin-film-based ferroelectric tunnel junction via stress induced crystallization. *Applied Physics Letters* **2020**, *117*, 242901.

[25] Fields, S. S.; Cai, T.; Jaszewski, S. T.; Salanova, A.; Mimura, T.; Heinrich, H. H.; Henry, M. D.; Kelley, K. P.; Sheldon, B. W.; Ihlefeld, J. F. Origin of Ferroelectric Phase Stabilization via the Clamping Effect in Ferroelectric Hafnium Zirconium Oxide Thin Films. *Advanced Electronic Materials* **2022**, *8*, 2200601.

[26] Jaszewski, S. T.; Fields, S. S.; Calderon, S.; Aronson, B. L.; Beechem, T. E.; Kelley, K. P.; Zhang, C.; Lenox, M. K.; Brummel, I. A.; Dickey, E. C.; et al. Phase Transformations Driving Biaxial Stress Reduction During Wake-Up of Ferroelectric Hafnium Zirconium Oxide Thin Films. *Advanced Electronic Materials* **2024**, *10*, 2400151.

[27] Lomenzo, P. D.; Richter, C.; Mikolajick, T.; Schroeder, U. Depolarization as Driving Force in Antiferroelectric Hafnia and Ferroelectric Wake-Up. *ACS Appl. Electron. Mater.* **2020**, *2*, 1583–1595.

[28] Xu, B.; Ganser, R.; Holsgrove, K. M.; Wang, X.; Vishnumurthy, P.; Mikolajick, T.; Schroeder, U.; Kersch, A.; Lomenzo, P. D. Influence of Biaxial Strain and Interfacial Layer Growth on Ferroelectric Wake-Up and Phase Transition Fields in ZrO_2. *ACS Appl. Mater. Interfaces* **2024**, *16*, 32533–32542.

[29] Hsain, H. A.; Lee, Y.; Lancaster, S.; Materano, M.; Alcala, R.; Xu, B.; Mikolajick, T.; Schroeder, U.; Parsons, G. N.; Jones, J. L. Role of Oxygen Source on Buried Interfaces in Atomic-Layer-Deposited Ferroelectric Hafnia–Zirconia Thin Films. *ACS Appl. Mater. Interfaces* **2022**, *14*, 42232–42244.

[30] Lomenzo, P. D.; Materano, M.; Mittmann, T.; Buragohain, P.; Gruverman, A.; Kiguchi, T.; Mikolajick, T.; Schroeder, U. Harnessing Phase Transitions in Antiferroelectric ZrO_2 Using the Size Effect. *Advanced Electronic Materials* **2022**, *8*, 2100556.

[31] Lomenzo, P. D.; Collins, L.; Ganser, R.; Xu, B.; Guido, R.; Gruverman, A.; Kersch, A.; Mikolajick, T.; Schroeder, U. Discovery of Nanoscale Electric Field-Induced Phase Transitions in ZrO_2. *Advanced Functional Materials* **2023**, *33*, 2303636.

[32] Müller, J.; Böscke, T. S.; Schröder, U.; Mueller, S.; Bräuhaus, D.; Böttger, U.; Frey, L.; Mikolajick, T. Ferroelectricity in Simple Binary ZrO_2 and HfO_2. *Nano Lett.* **2012**, *12*, 4318–4323.

[33] Fields, S. S.; Smith, S. W.; Ryan, P. J.; Jaszewski, S. T.; Brummel, I. A.; Salanova, A.; Esteves, G.; Wolfley, S. L.; Henry, M. D.; Davids, P. S.; et al. Phase-Exchange-Driven Wake-Up and Fatigue in Ferroelectric Hafnium Zirconium Oxide Films. *ACS Appl. Mater. Interfaces* **2020**, *12*, 26577–26585.

[34] Pešić, M.; Fengler, F. P. G.; Larcher, L.; Padovani, A.; Schenk,

Just Accepted

T.; Grimley, E. D.; Sang, X.; LeBeau, J. M.; Slesazeck, S.; Schroeder, U.; et al. Physical Mechanisms behind the Field-Cycling Behavior of HfO_2-Based Ferroelectric Capacitors. *Advanced Functional Materials* **2016**, *26*, 4601–4612.

[35] Lederer, M.; Olivo, R.; Lehninger, D.; Abdulazhanov, S.; Kämpfe, T.; Kirbach, S.; Mart, C.; Seidel, K.; Eng, L. M. On the Origin of Wake-Up and Antiferroelectric-Like Behavior in Ferroelectric Hafnium Oxide. *physica status solidi (RRL) – Rapid Research Letters* **2021**, *15*, 2100086.

[36] Lederer, M.; Lehninger, D.; Ali, T.; Kämpfe, T. Review on the Microstructure of Ferroelectric Hafnium Oxides. *Physica Rapid Research Ltrs* **2022**, *16*, 2200168.

[37] Pešić, M.; Hoffmann, M.; Richter, C.; Mikolajick, T.; Schroeder, U. Nonvolatile random access memory and energy storage based on antiferroelectric like hysteresis in ZrO_2. *Advanced Functional Materials* **2016**, *26*, 7486–7494.

[38] Park, M. H.; Kim, H. J.; Kim, Y. J.; Lee, Y. H.; Moon, T.; Kim, K. D.; Hyun, S. D.; Fengler, F.; Schroeder, U.; Hwang, C. S. Effect of Zr Content on the Wake-Up Effect in $Hf_{1-x}Zr_xO_2$ Films. *ACS Appl. Mater. Interfaces* **2016**, *8*, 15466–15475.

[39] Ramaswamy N.; Calderoni A.; Zahurak J.; Servalli G.; Chavan A.; Chhajed S.; Balakrishnan M.; Fischer M.; Hollander M.; Ettisserry D. P.; et al. NVDRAM: A 32Gb Dual Layer 3D Stacked Non-volatile Ferroelectric Memory with Near-DRAM Performance for Demanding AI Workloads. *2023 International Electron Devices Meeting (IEDM)* **2023**, 1–4.

[40] Park, M. H.; Kim, H. J.; Kim, Y. J.; Lee, W.; Moon, T.; Hwang, C. S. Evolution of phases and ferroelectric properties of thin $Hf_{0.5}Zr_{0.5}O_2$ films according to the thickness and annealing temperature. *Appl. Phys. Lett.* **2013**, *102*, 242905.

[41] Sunil, A.; Alcala, R.; Silva, C.; Mikolajick, T.; Lancaster, S. Controlling the Wake-Up Mechanism and Switching Kinetics of Ferroelectric $Hf_xZr_{1-x}O_2$ through Hf Content Modulation. *ACS Appl. Mater. Interfaces* **2025**, *17*, 62708–62719.

[42] Vishnumurthy, P.; Xu, B.; Wunderwald, F.; Richter, C.; Rehm, O.; Baumgarten, L.; Müller, M.; Mikolajick, T.; Kersch, A.; Schroeder, U. Impact of Hafnium Doping on Phase Transition, Interface, and Reliability Properties of $Zr_xHf_{1-x}O_2$-Based Capacitors. *ACS Appl. Electron. Mater.* **2024**, *6*, 6174–6185.

© The Author(s) 2026. *Nano Research* published by Tsinghua University Press. The articles published in this open access journal are distributed under the terms of the Creative Commons Attribution 4.0 International License (http://creativecommons.org/licenses/by/4.0/), which permits use, distribution and reproduction in any medium, provided the original work is properly cited.

Just Accepted

Electronic Supplementary Material

Overcoming the thickness scaling limit in hafnium-based ferroelectrics via interfacial strain and conductivity engineering

Bohan Xu[1,2,§], Florian Wunderwald[1, §], Kristina M. Holsgrove[3], Athira Sunil[1], Roberto Guido[1], Julie Laguerre[1], Pramoda Vishnumurthy[1], Xuetao Wang[1], Thomas Mikolajick[1,4], and Uwe Schroeder[1]

[1]*NaMLab gGmbH, Dresden 01187, Germany*
[2]*School of Integrated Circuits, Shandong University, Jinan 250100, China*
[3]*School of Mathematics and Physics, Queen's University Belfast, Belfast BT7 1NN, Northern Ireland, UK*
[4]*Chair of Nanoelectronics, TU Dresden, Dresden 01187, Germany*
[§] *Bohan Xu and Florian Wunderwald contributed equally to this work.*

Supporting information to https://doi.org/10.26599/NR.2026.94908815

Just Accepted

Address correspondence to Bohan Xu, bohanxu@sdu.edu.cn; Roberto Guido, roberto.guido@namlab.com; Uwe Schroeder,

Section S1: Sketch of the capacitor structures

As shown in **Figure S1**, the Pt/Ti dots serve as hard masks, the top and bottom electrodes are either TiN or W, and the bare top electrodes are etched out to form the capacitor structure. The capacitor area is 1960 μm^2 to prevent a strong RC delay effect.

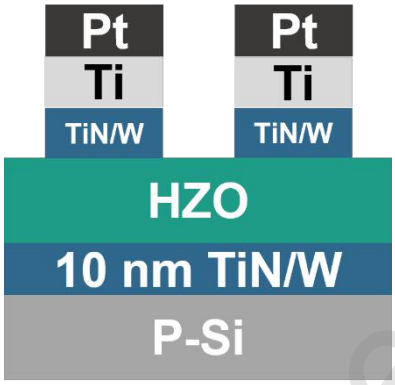

Figure S1 Schematic diagram of the capacitor structure with $Hf_{0.5}Zr_{0.5}O_2$ (HZO) films and TiN or W electrode.

Section S2: Bragg-Brentano Strain Measurements

Bragg's Brentano X-ray diffraction (BBXRD) measurements characterize the in-plane strain in HZO films. To ensure sufficient signal strength, an integration time of 150 seconds per point is applied during measurements, while a 1 mm collimator is used. By increasing the Ψ angle of the BBXRD measurements, the measured lattice spacing is changed from out-of-plane to in-plane. The lattice spacing is calculated using Bragg's equation:

$$d = \frac{n\cdot\lambda}{2sin\theta} \tag{S1}$$

where d is the d-spacing, n is the diffraction order (n = 1), and λ is the x-ray wavelength, which is 0.15418 nm. Based on the $\sin^2\Psi$ method [1,2], the relationship between strain and d-spacing can be described as:

$$x_{\phi,\Psi} = \frac{d_{\phi,\Psi} - d_0}{d_0} = x_{11}\cdot cos^2\phi\cdot sin^2\Psi + x_{12}\cdot \sin(2\phi)\cdot sin^2\Psi + x_{22}\cdot sin^2\phi\cdot sin^2\Psi - \quad x_{33}\cdot sin^2\Psi + x_{33} + x_{13}\cdot cos\phi\cdot \sin(2\Psi) + x_{23}\cdot sin\phi\cdot \sin(2\Psi) \tag{S2}$$

d_0 is the lattice spacing without any strain, x stands for the strain, σ is the stress, and the angle of ϕ, which is zero in this work. Moreover, by considering the state of in-plane rotational strain symmetry ($x_{11} = x_{22}$), and shear strain-free ($x_{12} = x_{13} = x_{23} = 0$) [3], it can be simplified as:

$$x_\Psi = \frac{d_\Psi - d_0}{d_0} = (x_{11} - x_{33})\cdot sin^2\Psi + x_{33} \tag{S3}$$

Because the out-of-plane dimension is much smaller than the in-plane dimension, it can be estimated that the in-plane stress is the sole reason for the strains observed. Therefore, the out-of-plane stress is assumed to be zero ($\sigma_{33} = 0$), and the out-of-plane strain and in-plane strain can be related with Poisson ratio ν as:

$$x_{33} = \frac{-2\cdot\nu}{(1-\nu)}\cdot x_{11} \tag{S4}$$

Therefore, by combining **Equations (S3)** and **(S4)**, the relation between the d-spacing d_Ψ and $sin^2\Psi$ can be described as:

$$d_\Psi = \frac{(1-\nu)\cdot x_{11}\cdot d_0}{1-\nu}\cdot sin^2\Psi + \left(1 + \frac{-2\cdot\nu}{(1-\nu)}\cdot x_{11}\right)\cdot d_0 \tag{S5}$$

Therefore, the in-plain strain (x_{11}) can be calculated based on the following equations:

$$x_{11} = x_{22} = \frac{(1-\nu)\cdot k}{(1+\nu)\cdot b + 2\cdot\nu\cdot k} \tag{S6}$$

Where ν is the Poisson's ratio, k and b are the slope and intercept of the least square regression lines, respectively. In this work, ν = 0.29 is applied for calculations. Therefore, the in-plane strain x_{11} can be calculated based on the relationship between the lattice spacing d_Ψ and $\sin^2\Psi$. It should be noted that the diffraction peaks

Just Accepted

of the t- phase and o- phase in HZO films are very close but not identical, and HfO_2 and ZrO_2 exhibit similar yet different lattice parameters. For this reason, the reference lattice parameters vary among different films, according to their elemental and phase compositions. However, the reference lattice parameter d_0 can still be determined for a specific film as:

$$d_0 = \frac{2 \cdot \nu \cdot k}{1+\nu} + b \tag{S7}$$

Section S3: Interfacial Layer Determination

The electric properties and effective thickness of the interfacial layer can be defined through impedance spectroscopy by appropriate circuit modeling with a Load-Load-Load (LLL) compensation sequence. For the LLL compensation sequence, three distinct resistors-1 MΩ, 3.6 kΩ, and 100 Ω were selected as reference loads. During the compensation sequence, the manipulator probes were connected to each load, and the frequency sweep was conducted from 1 Hz to 5 MHz at a zero DC bias. Compensation was performed sequentially for each load in the aforementioned frequency range. Using the built-in parasitic compensation capabilities of the Zurich Instruments MFIA Impedance Analyzer, the stray/parasitic capacitance and inductance of the cables and contact probes were measured. These parasitic elements were subsequently eliminated from the experimental measurements to ensure the dielectric response of the ferroelectric capacitor was accurately isolated.

With the TiO_xN_y as the interfacial layer, the impedance spectroscopy needs to employ a constant phase elements (CPE) model to simulate the interfacial layer, as illustrated in **Figure 2(c)**. The impedance of the CPE interface can be expressed as:

$$Z_{CTE} = \frac{1}{Q \cdot (j\omega)^n} \tag{S8}$$

where ω is angular frequency, and j is the imaginary unit, and Q and n are two CPE components for this module [4,5]. The effective capacitance of the interfacial layer can be calculated based on the CPE module as:

$$C_{eff} = \frac{(R \cdot Q)^{1/n}}{R} \tag{S9}$$

where R is the interface resistance. The interfacial layer thickness can be calculated as:

$$d = \frac{\varepsilon_0 \cdot \varepsilon_{int} \cdot A}{C_{eff}} \tag{S10}$$

where ε_{int} is the relative permittivity of the interfacial layer, which is estimated as 10. A is the capacitor area, which is $1.6 \cdot 10^{-9}$ m^2. **Table S1** presents the output parameters for 5-nm-thick HZO films with TiN electrodes based on this module, and two measurements have been conducted.

Table S1 Output parameters for 5-nm-thick HZO films with TiN electrodes.

Measurements	Bulk resistance (Ω)	Bulk capacitance (F)	Interface resistance (Ω)	Q_CPE	n_CPE	Interface effective capacitance (F)	Interface thickness (nm) ($\varepsilon_{int} \sim 10$)
1st	$4.29 \cdot 10^9$	$6.6 \cdot 10^{-9}$	548	$5.3 \cdot 10^{-9}$	0.99	$6.0 \cdot 10^{-9}$	2.3
2nd	$4.66 \cdot 10^9$	$6.6 \cdot 10^{-9}$	551	$5.6 \cdot 10^{-9}$	0.99	$6.4 \cdot 10^{-9}$	2.2

In contrast, With the WO_x as the interfacial layer, the impedance spectroscopy does not need the CPE model to simulate the interfacial layer, as illustrated in **Figure 2(d)**. It is also worth noting that, according to our previous work, the films do not normally degrade during impedance measurements [6–8].

Moreover, according to the characterizations from high-angle annular dark-field scanning transmission electron microscopy (HAADF-STEM) and energy-dispersive X-ray spectrometer (EDX), interfacial layers have been observed at the interface between electrodes and HZO films. The composition of this interfacial layer is TiO_xN_y between HZO and TiN electrode, and WO_x between HZO and TiN electrode.

Just Accepted

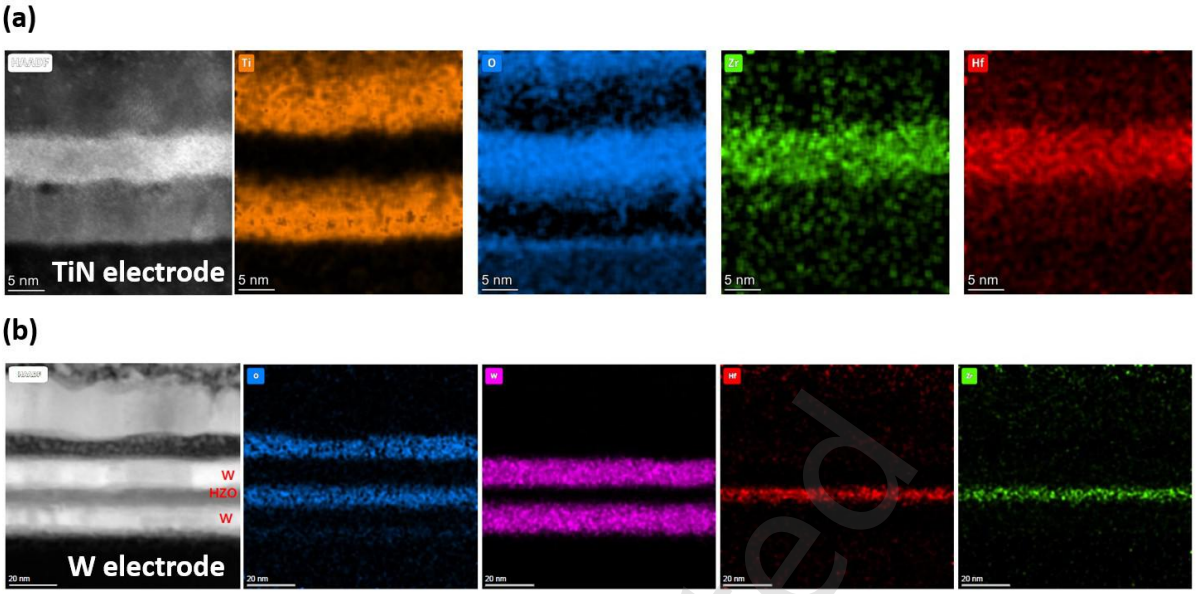

Figure S2 high-angle annular dark-field scanning transmission electron microscopy images and corresponding element distributions obtained by energy-dispersive X-ray spectrometer in the 5-nm-thick HZO films with (a) TiN electrodes and (b) W electrodes.

Section S4: Field Cycling Endurance

In FeRAM, the electric field cycling endurance is an important parameter to consider because an unlimited re-writing capability at the maximum operation frequency is required for random-access memories. Moreover, reading the state of the cells is a destructive operation in case of ferroelectric switching; therefore, half of the read cycles additionally contribute to the re-write endurance [9,10]. However, the cycling frequency and the magnitude of the applied electric field can significantly impact the endurance of HZO films. As illustrated in **Figure S3(a)**, the endurance of a 5 nm thick HZO film with W electrodes improves by increasing the frequency of the square electrical pulses used to cycle the capacitors, likely because increasing the cycling frequency corresponds to applying the voltage to the capacitor for increasingly shorter times after completing the polarization reversal. At a frequency of 100 kHz, the film survives $2{\cdot}10^5$ electric field cycles for 3 MV·cm^{-1} and $2{\cdot}10^4$ for 3.4 MV·cm^{-1}, respectively. The area of the capacitors is small enough to prevent a significant impact of the resistive-capacitive delay (for capacitor dot radius < 25 µm see **Figure S4**). However, a faster endurance increase compared to the initial trend is observed when increasing the frequency above 100 kHz for cycling at 3 MV·cm^{-1} or 1 MHz for 3.4 MV·cm^{-1}. Such a faster endurance increase can be explained considering that achieving complete switching at frequencies above 100 kHz requires to apply even higher electric fields > 3 MV·cm^{-1} (see **Figure S5**). For 3.4 MV·cm^{-1} complete switching can be achieved up to 1 MHz.

However, as shown in **Figure S3(b)**, increasing the applied electric field decreases the endurance of HZO films for both 5 and 10 nm thicknesses, whereas an improved endurance has been observed in thinner films. If the applied electric field is too low, the switching current in HZO films decreases, and complete polarization reversal might not be achieved (see **Figure S6**). Therefore, the applied voltage should be within an intermediate range that fulfills the requirements for both switching current and endurance. **Figure S3(c)** exhibits the $2P_r$ in 5 and 10 nm HZO with TiN or W electrodes. It is important to note that the applied electric field and frequency are fixed at 3 MV·cm^{-1} and 100 kHz, respectively. The applied electric fields are lower than those utilized for the measurements shown in **Figure 3**. Comparing the HZO films with TiN and W electrodes reveals that the films with TiN electrodes exhibit better endurance. However, it should be noted that, for the same applied electric

Just Accepted

field, HZO films with W electrodes exhibit larger P_r, as illustrated in **Figure S3(d)**. P_r is in saturation at 3.5 MV·cm^{-1} for W electrodes, but still increases for the TiN case. Hence, HZO films with TiN electrodes require a higher applied electric field magnitude to achieve comparable P_r values to those exhibited using W electrodes. This phenomenon can be attributed to the existence of the non-polar TiO_xN_y layer as well as the presence of larger in-plane tensile strain in the film. Indeed, the electric field partially drops on the dielectric TiO_xN_y interfacial layer, and therefore, a higher field is required to switch the HZO films.

In general, the HZO films with W electrodes exhibit better $2P_r$ but worse cycling endurance. However, it should be noted that it cannot be solely attributed to a trade-off between remanent polarization and cycling endurance. As shown in **Figure S3(b)**, the 5 nm HZO film with W electrodes exhibits better $2P_r$ combined with enhanced endurance compared to the 10 nm films. These observations indicate that electrode-dependent interfacial layer properties influence the endurance behavior. In films with TiN electrodes, the dielectric TiO_xN_y interfacial layer formed during device processing degrades during electric-field cycling, limiting endurance [11]. However, this interfacial layer can also serve as an oxygen diffusion barrier, suppressing oxygen vacancy formation within the HZO layer [12,13]. This mechanism enhances endurance despite the lower polarization typically observed. In contrast, W electrodes introduces conductive WO_x interfacial layers that facilitates oxygen scavenging from the HZO layer. This process generates excess oxygen vacancies, which promote accelerated dielectric breakdown electric field cycling, which is faster than the degradation of the TiO_xN_y interfacial layer. For resistive switching devices, enhanced oxygen scavenging is reported during field cycling [14].

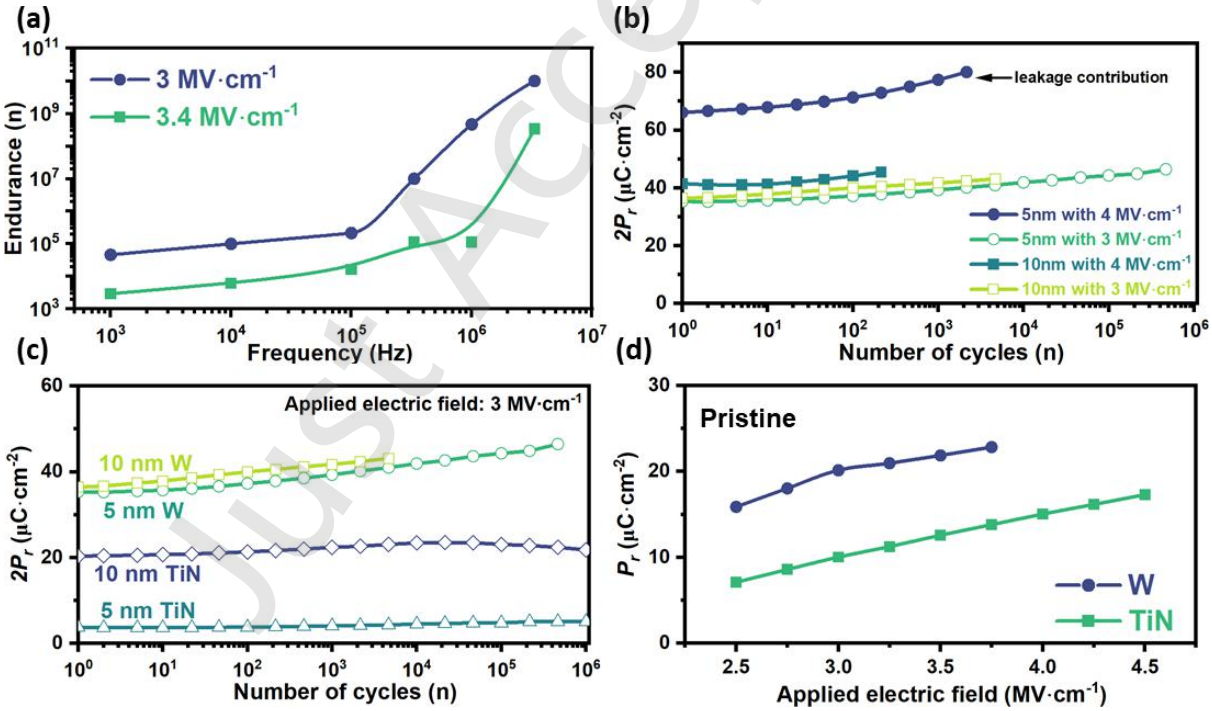

Figure S3 (a) Electric field cycling endurance versus frequency of the electrical cycling stimulus for a 5 nm thick HZO film with W electrodes and an applied electric field of 3 and 3.4 MV·cm^{-1}. (b) Two times remanent polarization ($2P_r$) versus number of electric field cycles for 5 and 10 nm thick HZO films with W electrodes. The measurements were performed with an applied electric field of either 3 or 4 MV·cm^{-1}, and at a frequency of 100 kHz. The contribution of the leakage current leads to the large P_r in the 5 nm HZO film measured at 4 MV·cm^{-1}. (c) $2P_r$ versus the number of electric field cycles for 5 and 10 nm thick HZO films with TiN or W electrodes. The measurements were carried out with 100 kHz frequency and 3 MV·cm^{-1} electric field. (d) P_r as a function of the applied electric field for pristine 10 nm thick HZO films with W or TiN electrodes.

As illustrated by the switching kinetics measurement results in **Figure S4**, to reach a remanent polarization of 15 μC·cm^{-2} in 7 nm thick HZO films with a capacitor area of 10000 μm^2, a resistive-capacitive delay (RC delay) starts to play an essential role in reducing the switching speed when the write/read pulse duration is less than

Just Accepted

2 μs (500 kHz in frequency). Once the capacitor area is reduced to 1960 μm^2, no significant RC delay effect is observed until the write/read pulse duration is 200 ns.

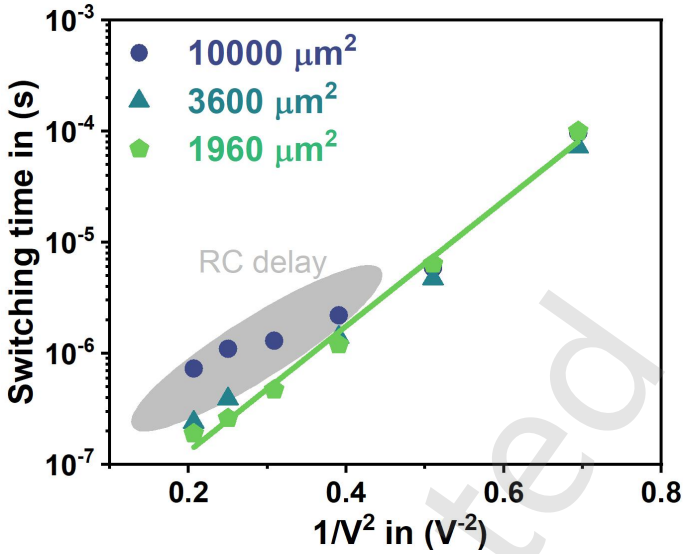

Figure S4 Switching time versus the reciprocal of squared voltage for 7 nm thick HZO films with W electrodes and different areas of the capacitors.

However, it can still be observed that the cycling frequency can affect the dynamic hysteresis loops. As illustrated in **Figure S5**, by increasing the cycling frequency from 1 to 4 MHz, an incomplete switching is observed, indicating that a larger applied electric field is required for the measurement at higher frequency for achieving full switching.

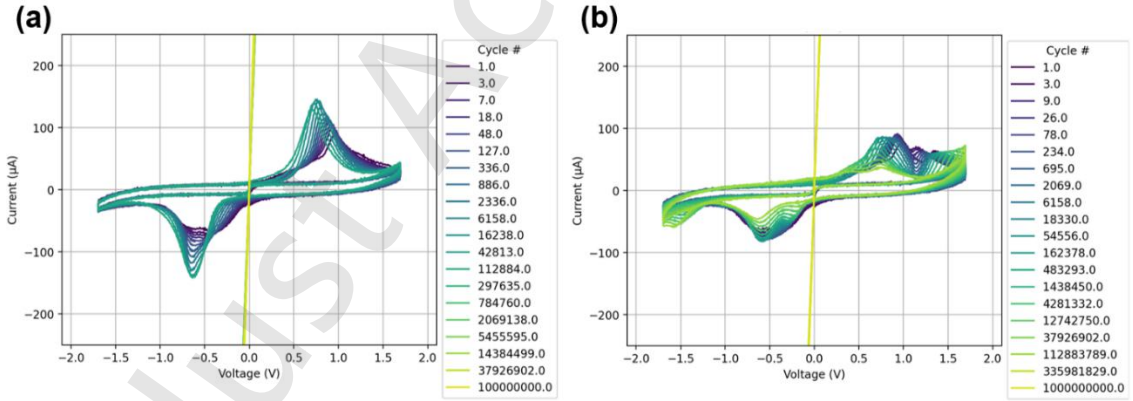

Figure S5 Current hysteresis loops for 5 nm thick HZO films with W electrodes measured with 3.4 MV·cm^{-1} with different number of cycles and cycling frequency of (a) 1 MHz and (b) 4 MHz.

As demonstrated in **Figure S6**, regardless of the electrode of the HZO films, whether TiN or W, a reduction in the applied electric field can diminish the switching current, rendering it too low to be detected by the devices.

Just Accepted

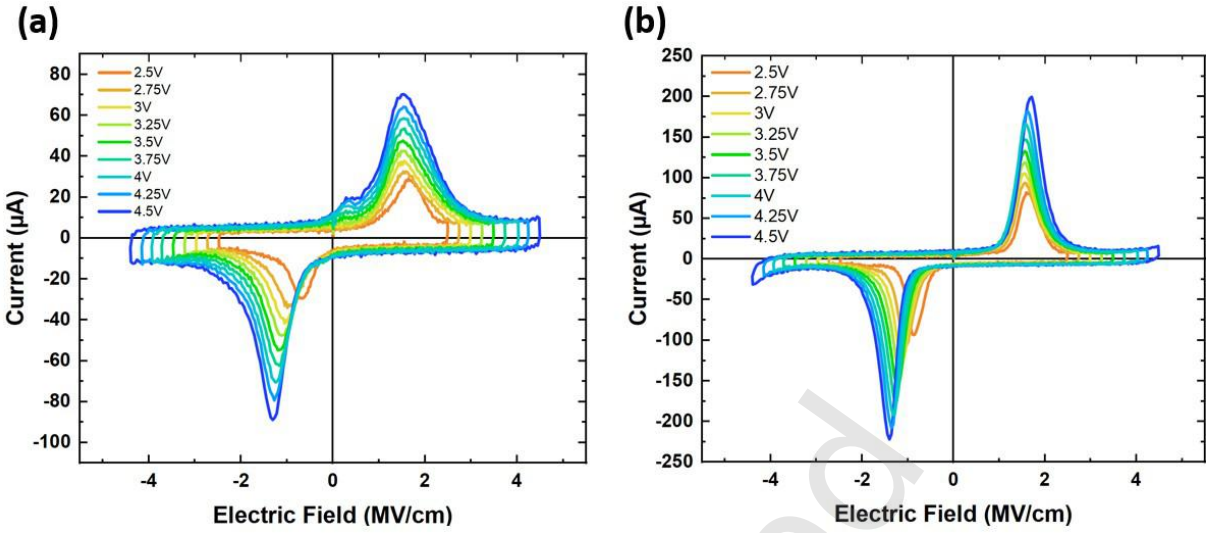

Figure S6 Currents versus electric field applied to 10 nm thick HZO films with **(a)** TiN and **(b)** W electrodes

Just Accepted

References

[1] Macherauch, E. X-ray stress analysis. *Experimental Mechanics* **1966**, *6*, 140–153.

[2] Noyan, I. C.; Huang, T. C.; York, B. R. Residual stress/strain analysis in thin films by X-ray diffraction. *Critical Reviews in Solid State and Materials Sciences* **1995**, *20*, 125–177.

[3] Schenk, T.; Fancher, C. M.; Park, M. H.; Richter, C.; Künneth, C.; Kersch, A.; Jones, J. L.; Mikolajick, T.; Schroeder, U. On the Origin of the Large Remanent Polarization in La:HfO_2. *Advanced Electronic Materials* **2019**, *5*, 1900303.

[4] Chang, B.-Y. Conversion of a Constant Phase Element to an Equivalent Capacitor. *J. Electrochem. Sci. Technol.* **2020**, *11*, 318–321.

[5] Gore, C. M.; White, J. O.; Wachsman, E. D.; Thangadurai, V. Effect of composition and microstructure on electrical properties and CO_2 stability of donor-doped, proton conducting $BaCe_{1-(x+y)}Zr_xNb_yO_3$. *J. Mater. Chem. A* **2014**, *2*, 2363–2373.

[6] Mehmood, F.; Alcala, R.; Vishnumurthy, P.; Xu, B.; Sachdeva, R.; Mikolajick, T.; Schroeder, U. Reliability Improvement from La_2O_3 Interfaces in $Hf_{0.5}Zr_{0.5}O_2$-Based Ferroelectric Capacitors. *Advanced Materials Interfaces* **2023**, *10*, 2202151.

[7] Xu, B.; Ganser, R.; Holsgrove, K. M.; Wang, X.; Vishnumurthy, P.; Mikolajick, T.; Schroeder, U.; Kersch, A.; Lomenzo, P. D. Influence of Biaxial Strain and Interfacial Layer Growth on Ferroelectric Wake-Up and Phase Transition Fields in ZrO_2. *ACS Appl. Mater. Interfaces* **2024**, *16*, 32533–32542.

[8] Vishnumurthy, P.; Xu, B.; Wunderwald, F.; Richter, C.; Rehm, O.; Baumgarten, L.; Müller, M.; Mikolajick, T.; Kersch, A.; Schroeder, U. Impact of Hafnium Doping on Phase Transition, Interface, and Reliability Properties of $Zr_xHf_{1-x}O_2$-Based Capacitors. *ACS Appl. Electron. Mater.* **2024**, *6*, 6174–6185.

[9] Mikolajick, T.; Slesazeck, S.; Mulaosmanovic, H.; Park, M. H.; Fichtner, S.; Lomenzo, P. D.; Hoffmann, M.; Schroeder, U. Next generation ferroelectric materials for semiconductor process integration and their applications. *Journal of Applied Physics* **2021**, *129*, 100901.

[10] Mikolajick, T.; Park, M. H.; Begon-Lours, L.; Slesazeck, S. From Ferroelectric Material Optimization to Neuromorphic Devices. *Advanced Materials* **2023**, *35*, 2206042.

[11] Vishnumurthy P.; Alcala R.; Mikolajick T.; Schroeder U.; L. Antunes A.; Kersch A. Ferroelectric HfO_2-based Capacitors for FeRAM: Reliability from Field Cycling Endurance to Retention (invited). *2024 IEEE International Reliability Physics Symposium (IRPS)* **2024**, pp 1–10.

[12] Park, M. H.; Schenk, T.; Fancher, C. M.; Grimley, E. D.; Zhou, C.; Richter, C.; LeBeau, J. M.; Jones, J. L.; Mikolajick, T.; Schroeder, U. A comprehensive study on the structural evolution of HfO2 thin films doped with various dopants. *J. Mater. Chem. C* **2017**, *5*, 4677–4690.

[13] Hsain, H. A.; Lee, Y.; Lancaster, S.; Materano, M.; Alcala, R.; Xu, B.; Mikolajick, T.; Schroeder, U.; Parsons, G. N.; Jones, J. L. Role of Oxygen Source on Buried Interfaces in Atomic-Layer-Deposited Ferroelectric Hafnia–Zirconia Thin Films. *ACS Appl. Mater. Interfaces* **2022**, *14*, 42232–42244.

[14] Alcala, R.; Materano, M.; Lomenzo, P. D.; Vishnumurthy, P.; Hamouda, W.; Dubourdieu, C.; Kersch, A.; Barrett, N.; Mikolajick, T.; Schroeder, U. The Electrode-Ferroelectric Interface as the Primary Constraint on Endurance and Retention in HZO-Based Ferroelectric Capacitors. *Advanced Functional Materials* **2023**, *33*, 2303261.